Transportation Research Part C 46 (2014) 46–64

Contents lists available at ScienceDirect

Transportation Research Part C

journal homepage: www.elsevier.com/locate/trc

Dynamics of connected vehicle systems with delayed acceleration feedback

Jin I. Ge *, Gábor Orosz

Department of Mechanical Engineering, University of Michigan, Ann Arbor, MI 48109, USA

ARTICLE INFO

Article history:
Received 4 March 2014
Received in revised form 28 April 2014
Accepted 28 April 2014

Keywords:
Connected cruise control (CCC)
Head-to-tail string stability
Acceleration feedback
Time delay
Robustness
DSRC

ABSTRACT

In this paper, acceleration-based connected cruise control (CCC) is proposed to increase roadway traffic mobility. CCC is designed to be able to use acceleration signals received from multiple vehicles ahead through wireless vehicle-to-vehicle (V2V) communication. We consider various connectivity structures in heterogeneous platoons comprised of human-driven and CCC vehicles. We show that inserting a few CCC vehicles with appropriately designed gains and delays into the flow, one can stabilize otherwise string unstable vehicle platoons. Exploiting the flexibility of ad-hoc connectivity, CCC can be applied in a large variety of traffic scenarios. Moreover, using acceleration feedback in a selective manner, CCC provides robust performance and remains scalable for large systems of connected vehicles. Our conclusions are verified by simulations at the nonlinear level.

1. Introduction

Advanced driver assistance systems (ADAS) have been developing rapidly in the last decade, leading to significantly improved passenger comfort and active safety of road vehicles. However, mobility of road traffic has not experienced similar transformation, as traffic jams still plague highways and major cities in the United States and around the world (Schrank et al., 2012). Mobility depends on the properties of individual vehicles as well as on their interactions, i.e., on the control strategies used to react to the motion of other vehicles. A control strategy that is based solely on local traffic information has limited ability to change the dynamics at the system level, which is necessary if one wishes to eliminate traffic congestion.

Past research has shown that maintaining smooth traffic flow is closely related to the so-called string stability of the local controllers that represents their ability to attenuate velocity fluctuations coming from the vehicles in front (Orosz et al., 2010). Human drivers who rely on distance and velocity information are typically unable to maintain string stability in the entire velocity range due to their reaction time (Zhang and Orosz, 2013). A possible solution may be to use adaptive cruise control (ACC) where the distance and the velocity difference between the vehicle and its predecessor is measured by radar and the vehicle is actuated accordingly. Since the delay in these systems is smaller than the human reaction time, controllers may be designed to ensure attenuation of velocity fluctuations, which results in string stable platoons if all vehicles are controlled by the same ACC algorithm. A past study (Davis, 2004) has shown that traffic jams can be suppressed in a mixed traffic of human-driven and ACC vehicles, when ACC vehicles constitute at least 20% of the traffic flow. However, the

* Corresponding author. Tel.: +7346479732.
E-mail address: gejin@umich.edu (J.I. Ge).

http://dx.doi.org/10.1016/j.trc.2014.04.014
0968-090X/

current ratio of ACC vehicles on the road is estimated to be orders of magnitude smaller than this. Consequently, the improvement of traffic efficiency through ACC systems is very limited.

In order to overcome the limitations of ACC systems, one may use information about the motion of more than one preceding vehicles that can be obtained through wireless vehicle-to-vehicle (V2V) communication, such as dedicated short range communication (DSRC). In this way, the performance of ACC controllers, particularly the string stability, may be improved. Such augmented ACC systems are often referred to as cooperative adaptive cruise control (CACC) (van Arem et al., 2006). Experimental work in integrating ACC systems and wireless communication dates back to the PATH program in 1997, when a platoon of eight cars performed longitudinal motion control with the help of inter-vehicle communication on a closed highway (Rajamani and Shladover, 2001). Since 2009, the SARTRE project has been experimenting with vehicle platoons where each following vehicle is driven automatically using signals sensed by radars and transmitted from a designated platoon leader (the first vehicle in the platoon) that is equipped with high-quality sensors and driven by a professional driver (Chan et al., 2012). In 2011, the grand cooperative driving challenge (GCDC) in the Netherlands implemented the idea of feedback from the vehicle immediately ahead and the platoon leader (van Nunen et al., 2012; Geiger et al., 2012; Lidström et al., 2012). These experiments pointed out the benefits of using signals received from vehicles farther ahead. However, it was required that all vehicles in the platoon were equipped with ACC and the connectivity structures were fixed relying on a prescribed platoon leader. Such assumptions not only restrict the application of CACC in real traffic but also limit the feedback design to a particular connectivity structure. Considering the low penetration of ACC vehicles and the additional requirements to create CACC systems, the chance that three or more of these vehicles get close to each other in traffic is extremely low. Two recent papers (Wang et al., 2014a,b) discuss different control setups and heterogeneity for CACC platoons by lowering the requirement on penetration rate. However, specific repetitive connectivity patterns are assumed where vehicles only monitor the motion of the vehicles ahead and immediately behind. Therefore, the benefits of using information from distant vehicles are not exploited and requiring fixed connectivity may limit modularity in the entire transportation system.

Connected cruise control (CCC) is proposed to resolve these problems, where ad hoc platoons can be formed based on the available communication and platoons may be heterogeneous, i.e., include human-driven vehicles that only transmit data or do not participate in the communication at all. In this scenario, the leader is considered to be the furthest vehicle ahead that transmits signals to the CCC vehicle, and this may be different for each CCC vehicle. Since this framework neither requires a designated platoon leader nor a fixed communication structure, it allows modular design that is scalable for large systems. Moreover, the flexibility in the connectivity structure permits CCC design that is robust against the uncertainties in the parameters of human drivers. In fact, even a CCC vehicle may be human-driven in which case the communication-based control acts as a driver assistance system. Indeed, CCC can also be used to supplement ACC, or even to substitute sensors like radars with communication.

CCC can be designed based on the various signals received via V2V communication, including distance, velocity, and acceleration. Distance and velocity information has been used frequently when designing ACC controllers, but acceleration is seldom used since it requires taking derivatives of (noisy) velocity signals generated by the sensors. On the other hand, human drivers often use acceleration signals provided by the taillights, but they cannot determine the exact deceleration value, and can only observe the taillight of the vehicle immediately ahead. Using accurate acceleration information from multiple vehicles ahead may enable the host vehicle to better respond to traffic conditions. In this paper, we consider an acceleration-based CCC design, where the host vehicle is actuated using acceleration information broadcasted by other vehicles and local headway and velocity information monitored by sensors or human drivers. Moreover, we propose a delay-based control design where both the gains and the delays are tuned in the feedback loop. We show that this design is robust against variations of human parameters (driver gains and driver reaction time) and we derive the ranges of feasible acceleration gains and delays that ensure string stability. It has been shown that acceleration feedback can be effective in other applications involving human reaction time, e.g., human balancing (Insperger et al., 2013).

The layout of the paper is the following. In Section 2, we introduce a general class of the nonlinear car-following models that can be used to describe CCC as well as conventional vehicles. This general class of models allow us to consider a large variety of communication structures where a few CCC vehicles are inserted into the platoon to exploit V2V information. In Section 3, we linearize the system about the uniform flow equilibrium and analyze the head-to-tail string stability for different communication structures. The linear stability results are summarized using stability charts and the results are verified at the nonlinear level using numerical simulations. We conclude our results in Section 4.

2. Connected car-following models with acceleration feedback

We consider a platoon of $n+m+1$ vehicles traveling on a single lane as shown in Fig. 1(a). The preceding $n+m$ vehicles are not equipped with CCC and are assumed to be human-driven. The tail vehicle (the last vehicle of the platoon) implements acceleration-based CCC using acceleration signals received through V2V communication from n preceding vehicles. The car-following dynamics of the CCC vehicle is modeled by

$$\begin{aligned} \dot{h}(t) &= v_1(t) - v(t), \\ \dot{v}(t) &= \alpha\Big(V(h(t-\tau)) - v(t-\tau)\Big) + \beta\,\dot{h}(t-\tau) + \sum_{k=1}^{n}\gamma_k\,\dot{v}_k(t-\sigma_k), \end{aligned} \tag{1}$$

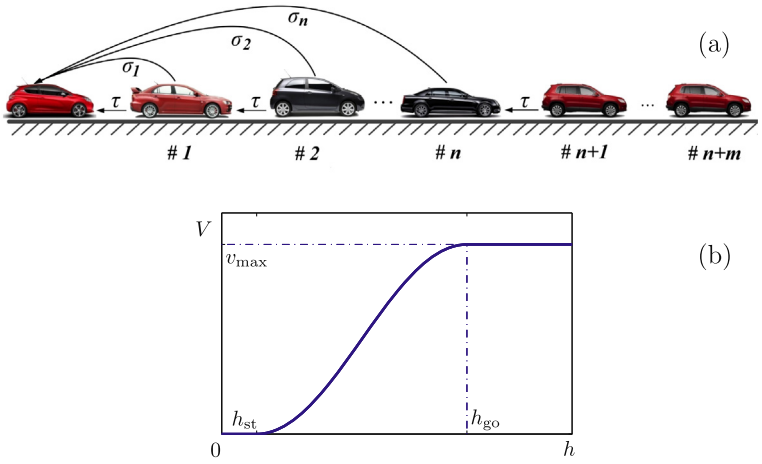

Fig. 1. (a) A heterogeneous vehicle platoon of $n+m+1$ vehicles with $n+m$ non-CCC vehicles and a CCC vehicle at the tail. The delays are indicated along the links. (b) The nonlinear range policy (2) used in this paper.

which can be obtained as a simplification of the physics-based model presented in Orosz (2014) and Orosz and Shah (2012). Here the dot stands for differentiation with respect to time t, h is the headway, i.e., the distance between the CCC vehicle and the vehicle immediately ahead, v is the velocity of the CCC vehicle, while $v_k, k=1,\ldots,n$ denotes the velocities of the preceding vehicles. The gains α and β are used for the headway and relative velocity, while τ represents the driver reaction time (0.5 – 1 [s]) or the sensing delay of the automated system (0.05 – 0.2 [s]). The gains and the delays for the acceleration signals are denoted by γ_k and $\sigma_k, k=1,\ldots,n$. Note that σ_k represents the sum of communication delay and human reaction time when CCC is used to warn the human driver, while it stands for the sum of communication delay and the delay in the controller when CCC is used to actuate the vehicle. We emphasize that in the latter case CCC can either be used to assist the human driver or to fully actuate the longitudinal dynamics of the vehicle. Even though wireless V2V communication can be considered to be instantaneous, communication delay of magnitude 0.1 – 0.4 [s] is reported due to the intermittencies and packet drops (Bai and Krishnan, 2006), that shall be incorporated in the σ_k – s.

In model (1), the acceleration of the CCC vehicle is determined by three terms: the difference between the desired velocity and the actual velocity, the velocity difference between the vehicle immediately ahead and the host vehicle, and the acceleration of multiple vehicles ahead. The desired velocity is determined by the headway using the range policy

$$V(h)=\begin{cases} 0 & \text{if} \quad h \leqslant h_{\rm st}, \\ \frac{v_{\max}}{2}\left(1-\cos\left(\pi\frac{h-h_{\rm st}}{h_{\rm go}-h_{\rm st}}\right)\right) & \text{if} \quad h_{\rm st}<h<h_{\rm go}, \\ v_{\max} & \text{if} \quad h \geqslant h_{\rm go}, \end{cases} \tag{2}$$

that is depicted in Fig. 1(b). This represents that when the headway is small ($h<h_{\rm st}$) the vehicle aims to stop, for large headway ($h>h_{\rm go}$) the vehicle aims to travel with maximum speed $v_{\max}$, and between these the desired velocity increases with the headway monotonically. Here we consider $v_{\max}=30$ [m/s], $h_{\rm st}=5$ [m], $h_{\rm go}=35$ [m] that corresponds to realistic traffic data (Orosz et al., 2010). Notice that function (2) and its derivative are continuous at $h_{\rm st}$ and $h_{\rm go}$, which ensures smooth longitudinal dynamics even in the jerk. Indeed, many other range policies may be chosen (Orosz et al., 2010), but the qualitative dynamics remain similar if the above characteristics are kept.

The driving behavior of the preceding non-CCC vehicles is described by the car-following model

$$\begin{aligned} \dot{h}_i(t) &= v_{i+1}(t)-v_i(t), \\ \dot{v}_i(t) &= \alpha\Big(V(h_i(t-\tau))-v_i(t-\tau)\Big)+\beta\,\dot{h}_i(t-\tau), \end{aligned} \tag{3}$$

where $i=1,\ldots,n+m$. For simplicity, we consider that all drivers are identical and that CCC is used as a driver assistance system. Thus (1) and (3) contain the same range policy $V(h)$, headway gain α, relative velocity gain β, and driver reaction time τ. To evaluate the robustness of our acceleration-based CCC design against uncertainties in driver parameters, we will investigate the dynamics for different values of α, β, and τ. On the other hand, the acceleration gains γ_k and delays σ_k will be used as design parameters. Indeed, these delays have minimal values as explained above, but we will show that they may be increased intentionally in order to obtain desired performance.

The longitudinal stability of a connected vehicle system includes plant stability and string stability. For the CCC vehicle, plant stability is defined as follows. Suppose that the vehicles whose signals are used by the CCC vehicle are driven at the same constant velocity. Then the CCC vehicle is plant stable if its velocity approaches this constant velocity. Consequently,

a platoon is said to be plant stable, if all vehicles approach the velocity of the head vehicle (the first vehicle in a platoon) when it is driven at a constant velocity.

Broadly speaking, string stability is achieved when velocity fluctuations are attenuated as they propagate upstream (Seiler et al., 2004). In predecessor-follower systems, where each vehicle reacts to the motion of the vehicle immediately ahead, string stability can be ensured by considering pairs of successive vehicles. However, this may not be suitable when incorporating CCC vehicles, whose control law depends on several preceding vehicles in the platoon. Moreover, many vehicles in the platoon can be purely human-driven, and their string stability cannot be ensured. Thus, the string stability of heterogeneous platoons containing CCC and conventional vehicles cannot be simplified to the string stability of pairs of successive vehicles. Here, we define the head-to-tail string stability and compare the velocity fluctuations of the head vehicle and the tail vehicle (that is assumed to be a CCC vehicle without loss of generality). This way, all the influences on the tail vehicle's motion are considered and we are able to compare the string stability of platoons with different structures of connectivity that may include multiple CCC vehicles. Notice that this definition allows that some vehicles in the platoon may amplify the velocity fluctuations of the head vehicle, but fluctuations are attenuated when they reach the tail.

3. Head-to-tail string stability for connected vehicle configurations

In this section, we focus on the dynamics of the connected vehicle system (1, 3) in the vicinity of an equilibrium that is achieved when all vehicles travel with the same constant velocity and maintain constant headways. While the equilibrium velocity v^* is determined by the head vehicle, the equilibrium headway h_i^* is obtained for each vehicle using the range policy $v^* = V_i(h_i^*)$. Since the range policies are assumed to be identical, here we obtain the uniform flow equilibrium

$$\begin{aligned} h(t) &\equiv h_i(t) = h^*, \\ v(t) &\equiv v_i(t) = v^* = V(h^*), \end{aligned} \tag{4}$$

for $i = 1, \dots, n+m$, where the vehicles are equidistant.

We define headway perturbations $\tilde{h}(t) = h(t) - h^*, \tilde{h}_i(t) = h_i(t) - h^*$ and the velocity perturbations $\tilde{v}(t) = v(t) - v^*, \tilde{v}_i(t) = v_i(t) - v^*, i = 1, \dots, n+m$, and linearize (1, 3) about the equilibrium (4). This yields

$$\begin{aligned} \dot{\tilde{h}}(t) &= \tilde{v}_1(t) - \tilde{v}(t), \\ \dot{\tilde{v}}(t) &= \alpha\Big(f^*\tilde{h}(t-\tau) - \tilde{v}(t-\tau)\Big) + \beta\, \dot{\tilde{h}}(t-\tau) + \sum_{k=1}^{n} \gamma_k\, \dot{\tilde{v}}_k(t-\sigma_k), \end{aligned} \tag{5}$$

for the CCC vehicle and

$$\begin{aligned} \dot{\tilde{h}}_i(t) &= \tilde{v}_{i+1}(t) - \tilde{v}_i(t), \\ \dot{\tilde{v}}_i(t) &= \alpha\Big(f^*\tilde{h}_i(t-\tau) - \tilde{v}_i(t-\tau)\Big) + \beta\, \dot{\tilde{h}}_i(t-\tau), \end{aligned} \tag{6}$$

for the other vehicles $i = 1, \dots, n+m$. Here $f^* = V'(h^*)$ is the derivative of the range policy at the equilibrium $h = h^*$ and the corresponding time headway is $t_h = 1/f^*$. It was shown in Orosz et al. (2010) that having larger f^* (i.e., smaller t_h) typically poses stricter conditions on string stability. In this paper, we use $(h^*, v^*) = (20\,[\mathrm{m}], 15\,[\mathrm{m/s}])$, which results in the maximum slope $f^* = \pi/2$ [1/s] corresponding to the minimum time headway $t_h = 2/\pi$ [s] (cf. (2) with $v_{\max} = 30$ [m/s], $h_{st} = 5$ [m], and $h_{go} = 35$ [m]).

We consider the velocity perturbation $\tilde{v}_{n+m}$ of the head vehicle as the input and the velocity perturbation $\tilde{v}$ of the tail vehicle as the output. Taking the Laplace transform of the system (5, 6) with zero initial conditions, and eliminating the velocities of the other vehicles and the headways, we obtain the head-to-tail transfer function

$$\Gamma(s) = \frac{\widetilde{V}(s)}{\widetilde{V}_{n+m}(s)} = \left(\frac{F(s)}{G(s)}\right)^{n+m} \left(1 + \sum_{k=1}^{n} \frac{F_k(s)(G(s))^{k-1}}{(F(s))^k}\right). \tag{7}$$

Here $\widetilde{V}(s)$ and $\widetilde{V}_{n+m}(s)$ denote the Laplace transform of $\tilde{v}(t)$ and $\tilde{v}_{n+m}(t)$, respectively, and we have

$$\begin{aligned} F(s) &= \beta s + \alpha f^*, \\ F_k(s) &= \gamma_k s^2\, \mathrm{e}^{(\tau-\sigma_k)s}, \\ G(s) &= s^2\, \mathrm{e}^{\tau s} + (\alpha+\beta)s + \alpha f^*. \end{aligned} \tag{8}$$

We remark that without V2V communication ($\gamma_k = 0 \Rightarrow F_k(s) = 0, k = 1, \dots, n$), the second term in (7) disappears and the transfer function degrades to $(F(s)/G(s))^{n+m}$, representing a platoon of human-driven vehicles.

Plant stability is determined by the denominator of the transfer function (7), that is, by $G(s)$ in (8), and it is influenced only by the driver parameters α, β, and τ. That is, the acceleration feedback does not improve the plant stability in this simple model. The system is linearly plant stable if and only if all solutions of the characteristic equation $G(s) = 0$ are located in the left half complex plane. One may substitute $s = \mathrm{i}\Omega, \Omega \geqslant 0$ into the characteristic equation, separate the real and imaginary parts, and obtain the plant stability boundary in parametric form:

$$\begin{aligned}\alpha &= \tfrac{\Omega^2}{f^*}\cos(\Omega\tau),\\ \beta &= \tfrac{\Omega}{f^*}(f^*\sin(\Omega\tau) - \Omega\cos(\Omega\tau)).\end{aligned} \tag{9}$$

In the following sections, we will depict this boundary using a circled curve when applicable. In most cases, the car-following model is plant stable, and we can focus on string stability.

Since perturbation signals can be represented using Fourier component, and superposition holds for linear systems, head-to-tail string stability is ensured when sinusoidal signals are attenuated between the head and the tail vehicles for all excitation frequencies. Therefore, at the linear level the necessary and sufficient condition for head-to-tail string stability is given by

$$P(\omega) = |\Gamma(\mathrm{i}\omega)|^2 - 1 < 0, \quad \forall\omega > 0, \tag{10}$$

where $\Gamma(\mathrm{i}\omega)$ is as defined by (7, 8). Since string stability is violated when the maximum of $P(\omega)$ is larger than 0, the stability boundary is given by the equations

$$\begin{aligned}&P(\omega^{\mathrm{cr}}) = 0,\\ &\tfrac{\partial P(\omega^{\mathrm{cr}})}{\partial\omega} = 0,\end{aligned} \tag{11}$$

subject to $\frac{\partial^2 P(\omega^{\mathrm{cr}})}{\partial\omega^2} < 0$, where ω^{cr} indicates the location of the maximum of $P(\omega)$. Note that $P(\omega)$ also depends on the system parameters $\alpha, \beta, \tau, \gamma_k, \sigma_k, k = 1,\dots,n$, but they are not spelled out in (10, 11) for the sake of simplicity. To generate string stability boundaries in the (γ_k,α)-plane, we fix the other parameters and solve (11) for $(\gamma_k(\omega^{\mathrm{cr}}), \alpha(\omega^{\mathrm{cr}}))$. Since it is not possible to solve (11) analytically, we use the continuation package DDE-BIFTOOL (Engelborghs et al., 2001) to obtain numerical solutions while varying the critical frequency ω^{cr}. In fact, we search for the equilibria of the mock differential equation

$$\begin{aligned}\dot\gamma_k &= P(\alpha,\gamma_k;\omega^{\mathrm{cr}}),\\ \dot\alpha &= \tfrac{\partial P(\alpha,\gamma_k;\omega^{\mathrm{cr}})}{\partial\omega},\end{aligned} \tag{12}$$

that satisfy $\frac{\partial^2 P(\alpha,\gamma_k;\omega^{\mathrm{cr}})}{\partial\omega^2} < 0$. First, for a specific ω^{cr}, an initial guess for α and γ_k is corrected by the Newton–Raphson method. Then the obtained solution is used as initial guess for nearby values of ω^{cr}. This way the solution can be continued, and $\gamma(\omega^{\mathrm{cr}})$ and $\alpha(\omega^{\mathrm{cr}})$ can be obtained numerically.

Substituting $\omega^{\mathrm{cr}} = 0$ into Eqs. (7, 8, and 11). We obtain $P(0) = 0$ and $\frac{\partial P(0)}{\partial\omega} = 0$. Thus, for zero frequency we require

$$\frac{\partial^2 P(0)}{\partial\omega^2} = -(n+m)(\alpha+2\beta) + 2f^*\left(n+m-\sum_{k=1}^{n}\gamma_k\right) < 0, \tag{13}$$

which is a necessary condition for string stability.

3.1. Monitoring the vehicle immediately ahead

First, we consider the case when the CCC vehicle only receives acceleration signals from the vehicle immediately ahead, i.e., $n = 1, m = 0$ in (1, 3) cf. Fig. 2(a). In this case, (7, 8) result in

$$\Gamma(s) = \frac{\widetilde V(s)}{\widetilde V_1(s)} = \frac{\gamma_1 s^2 \mathrm{e}^{(\tau-\sigma_1)s} + \beta s + \alpha f^*}{s^2\mathrm{e}^{\tau s} + (\alpha+\beta)s + \alpha f^*}, \tag{14}$$

and the string stability condition (10) can be written as

$$P(\omega) = (\gamma_1^2-1)\omega^4 + 2((\alpha+\beta)\sin(\tau\omega) - \beta\gamma_1\sin((\tau-\sigma_1)\omega))\omega^3 - \alpha(\alpha+2\beta-2f^*\cos(\tau\omega) + 2f^*\gamma_1\cos((\tau-\sigma_1)\omega))\omega^2 < 0. \tag{15}$$

For $\omega^{\mathrm{cr}} > 0$ the corresponding boundaries are given by (11), while for $\omega^{\mathrm{cr}} \to 0$ (13) gives the conditions

$$\alpha > 2(-\beta + f^*(1-\gamma_1)), \tag{16}$$

$$\alpha > 0. \tag{17}$$

As the acceleration gain γ_1 varies, the range of string stable parameters change for the gains α, β and the delays τ, σ_1. Here we fix the velocity gain $\beta = 0.9$ [1/s] and show this change using stability charts in the (γ_1,α)-plane for different values of the delays τ, σ_1 in Fig. 2. The string stability boundaries (11, 15, 16 and 17) are plotted as black curves enclosing the gray string stable area. The dashed lines in Fig. 2(c, e, g) show the sections of (16) that do not bound the string stable domains. Parameters outside the gray area result in that the transfer function (14) has magnitude larger than 1 at certain frequency ranges, which is represented by a color code: deep blue indicates low frequency and dark red indicates high frequency. More precisely, we solve (15) for frequencies $\omega_j^{\mathrm{p}} > 0, j = 1,2,\dots$ satisfying $P(\omega_j^{\mathrm{p}}) = |\Gamma(\mathrm{i}\omega_j^{\mathrm{p}})| - 1 = 0$ and color the points in the (γ_1,α)-plane according to the largest ω_j^{p}. In the vicinity of the string stability boundary, the color corresponds to the frequency at which string stability is lost.

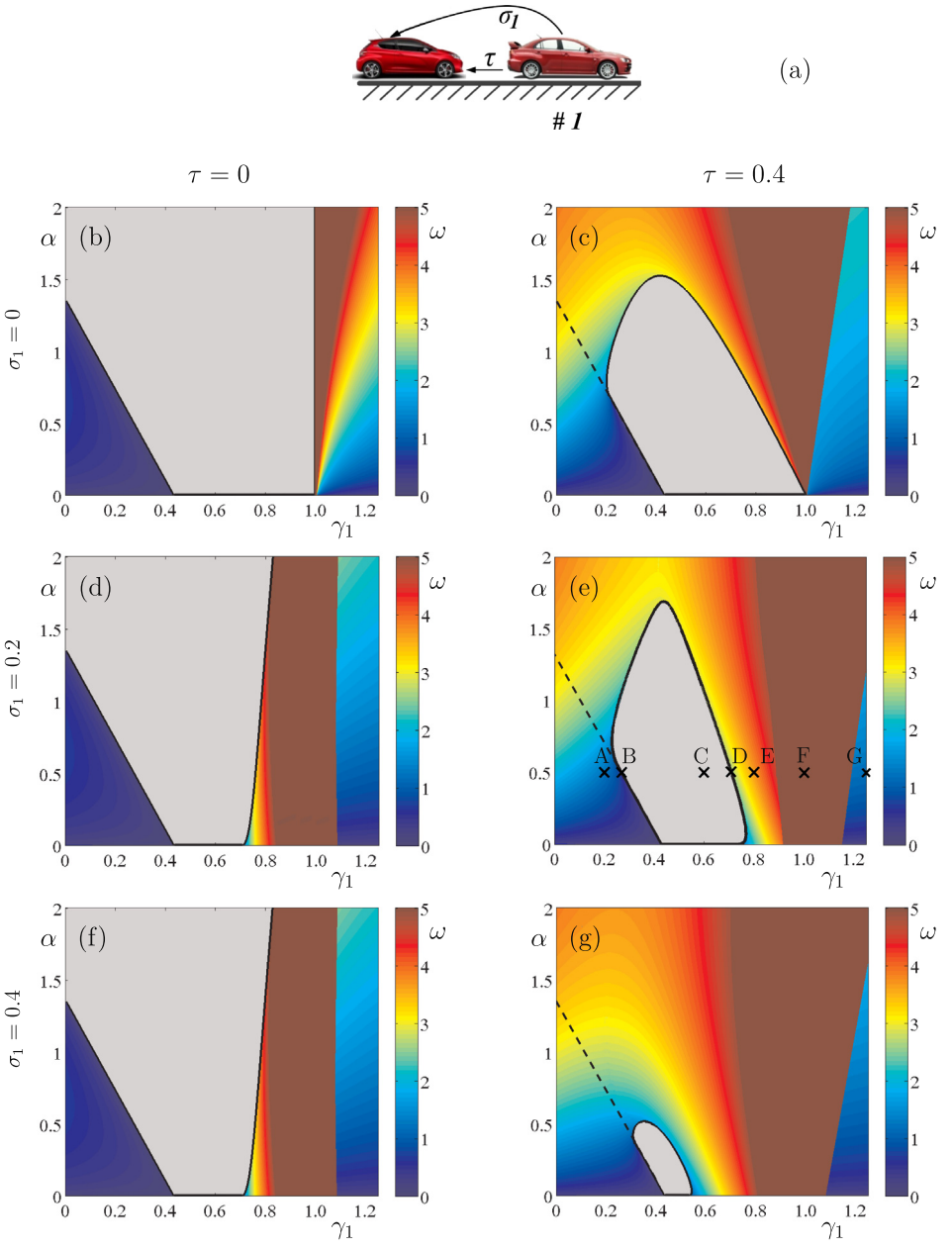

Fig. 2. (a) Connectivity structure for a single look-ahead platoon when a CCC vehicle monitors the car immediately ahead (i.e., $n = 1, m = 0$). The delays are indicated along the links. (b–g) String stability diagrams in the (γ_1, α)-plane for velocity gain $\beta = 0.9$ [1/s] and different driver reaction times τ and acceleration delays σ_1 as indicated. The gray areas are string stable. The color represents the highest frequency of string stability changes. The dashed lines in panels (b, d, f) represent the section of (16) that does not bound the string stable domain. (For interpretation of the references to color in this figure legend, the reader is referred to the web version of this article.)

Fig. 2(b, d, f) depicts the stability charts for $\tau = 0$, i.e., when the driver reaction time is omitted. In this case, for small values of γ_1, the string stability condition is given by (16), that is, string stability may be obtained by choosing sufficiently large α. When $\gamma_1 = 0$, we need $\alpha > 2(f^* - \beta)$. As γ_1 increases, the required α decreases and becomes zero at $\gamma_1 = 1 - \beta/f^*$. This boundary is independent of acceleration delay σ_1 as can be seen when comparing Fig. 2(b, d, f). In the vicinity of this boundary, deep blue color indicates that string stability is lost at low frequency $\omega^{cr} \to 0$. On the other hand, large γ_1 results in string instability for high frequencies, as indicated by the dark red domains at the right side of Fig. 2(b, d, f). This boundary is at $\gamma_1 = 1$ when $\sigma_1 = 0$ (Fig. 2(b)), and it moves to the left decreasing the string stable domain as the acceleration delay σ_1 increases (Fig. 2(d, f)).

As shown in Fig. 2(c, e, g), the string stable area shrinks significantly when choosing realistic driver reaction time $\tau = 0.4$ [s]. In this case, the string stability can be maintained when choosing $\gamma_1 \approx 0.5$, but there is no string stable domain without

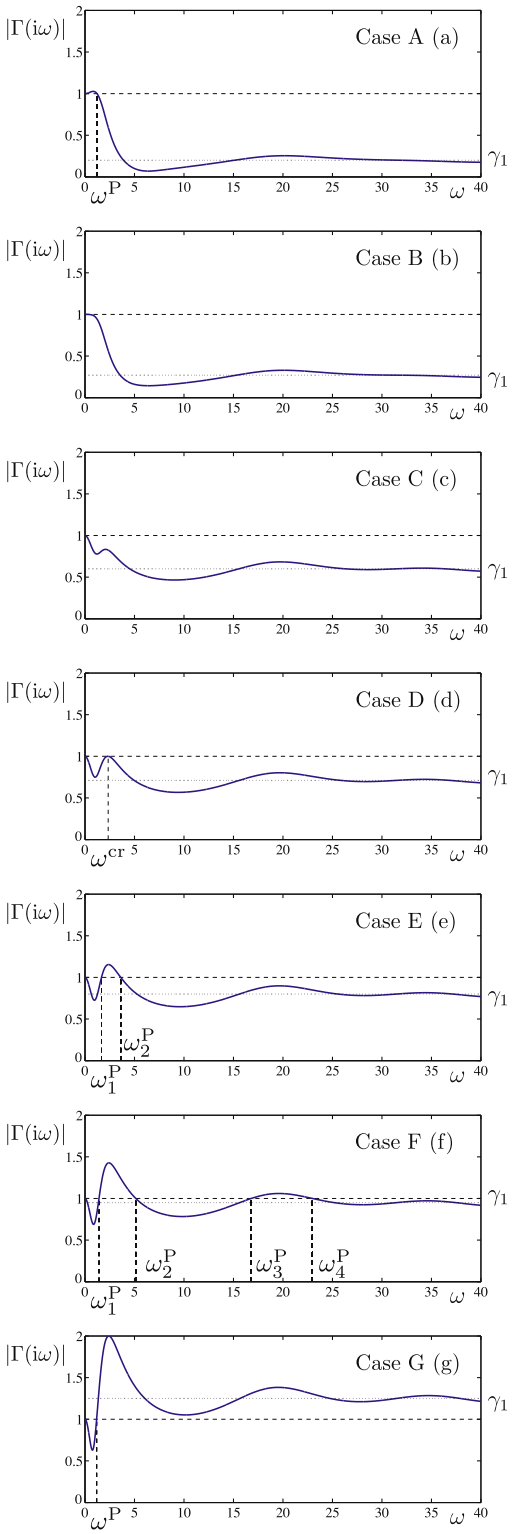

Fig. 3. Magnitude of the transfer function when a CCC vehicle monitors the car immediately ahead (i.e., $n = 1, m = 0$) for the points marked (A–G) in Fig. 2(e). The horizontal dashed line at 1 indicates the threshold for string stability. The horizontal dotted line shows the magnitude of transfer function when the frequency approaches infinity.

acceleration feedback ($\gamma_1 = 0$). In fact, in the latter case the system is string unstable for all choices of human parameters α and β, since τ exceeds a critical delay time as will be discussed below. As the acceleration delay σ_1 increases, the string stability domain shrinks and disappears at $\sigma_1 \approx 0.55$ [s]. The critical frequencies of string stability loss are still low on the left and high on the right side, as can be seen from the coloring of the string unstable domains.

To illustrate the stability loss at different critical frequencies, we mark the points A–G in Fig. 2(e) and and plot the magnitude of the transfer function $\Gamma(\mathrm{i}\omega)$ in Fig. 3 (cf. (14)). Comparing cases A, B and C, one can observe a string stability loss at low frequency ($\omega^{\mathrm{cr}} \to 0$). In case A, the system is string unstable for low frequencies $\omega < \omega^{\mathrm{P}} \approx 1.22$ [rad/s] (Fig. 3(a)), which corresponds to the blue color at A in Fig. 2(e). Point B is located at the string stability boundary (Fig. 3(b)), that is, $\frac{\partial^2|\Gamma(0)|}{\partial\omega^2} = 0$ (cf. (10), (13)), while the system is string stable in case C as shown in Fig. 3(c). Comparing cases C, D and E, a string stability loss at higher frequency can be observed. Point D is located at the string stability boundary, that is, $\Gamma(\omega^{\mathrm{cr}}) = 1, \frac{\partial|\Gamma(\omega^{\mathrm{cr}})|}{\partial\omega} = 0$ (cf. (10), (11)) where $\omega^{\mathrm{cr}} \approx 2.34$ [rad/s]. In case E, the system is string unstable in the frequency domain $\omega_1^{\mathrm{P}} < \omega < \omega_2^{\mathrm{P}}$ (Fig. 3(e)) and the orange color at point E in Fig. 2(e) corresponds to the higher frequency $\omega_2^{\mathrm{P}} \approx 3.61$ [rad/s].

Notice that as $\omega \to \infty$, the magnitude of the transfer function approaches γ_1, i.e., $\lim_{\omega\to\infty}|\Gamma(\mathrm{i}\omega)| = \gamma_1$ (cf. (14)), which is indicated by the dotted horizontal lines in Fig. 3. Therefore, as $\gamma_1 \to 1^-$, string instabilities appear in higher frequency ranges. This is demonstrated in Fig. 3(f) where the system is string unstable for $\omega_1^{\mathrm{P}} < \omega < \omega_2^{\mathrm{P}}$ and $\omega_3^{\mathrm{P}} < \omega < \omega_4^{\mathrm{P}}$. The dark red color at point F in Fig. 2(e) corresponds to the highest frequency $\omega_4^{\mathrm{P}} \approx 22.97$ [rad/s]. Finally we remark that when $\gamma_1 > 1$ the system becomes unstable for almost all frequencies as demonstrated in Fig. 3(g), where the system is unstable for $\omega > \omega^{\mathrm{P}} \approx 1.18$ [rad/s], which corresponds to the coloring at G in Fig. 2(e).

Now we evaluate the robustness of the design against uncertainties of the human gains α and β. In the right panels of Fig. 2, it can be observed that the stable regions cover the largest α interval for $\gamma_1 \approx 0.5$. Moreover, when every packet is delivered, DSRC communication has the average communication delay $\sigma_1 = 0.15$ [s], which goes up to $\sigma_1 = 0.2$ [s] when every second packet is lost (Qin et al., 2013; Qin et al., 2014). To evaluate the robustness, we use $\gamma_1 = 0.5$ and $\sigma_1 = 0.2$

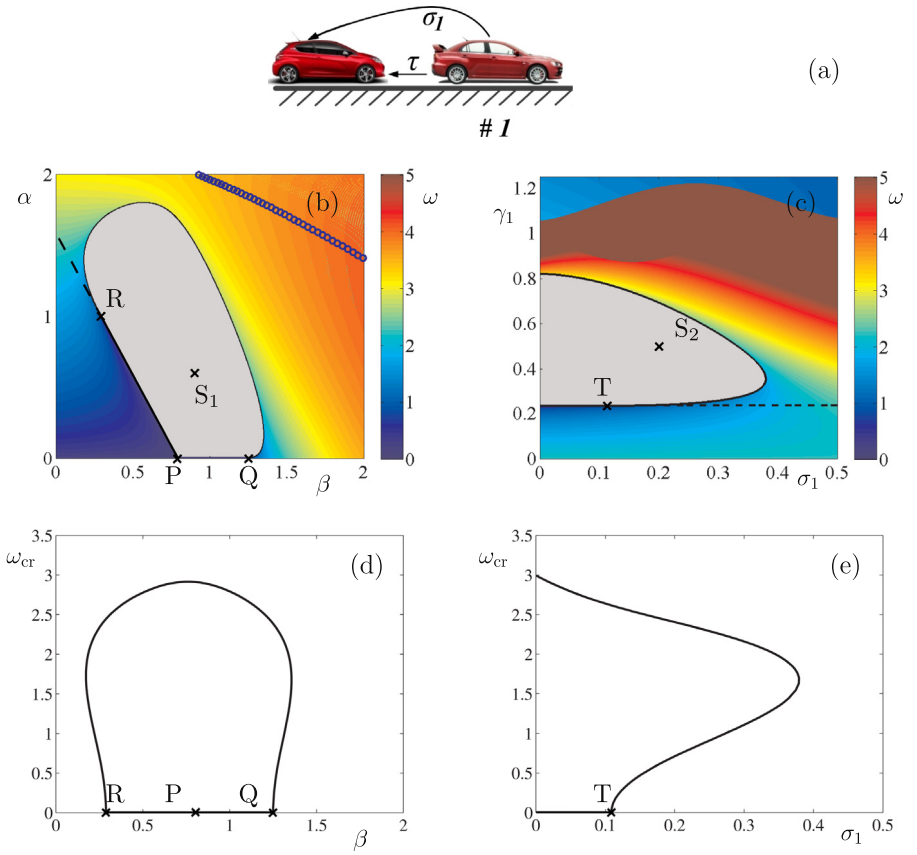

Fig. 4. (a) Connectivity structure for a single look-ahead platoon with delays indicated along the links. (b and c) String stability diagrams in the (β, α)-plane and (σ_1, γ_1)-plane for $\tau = 0.4$ [s]. In panel (b), points P, Q and R locate the intersections of (16), (17) and (11), (15), while S_1 is located at $(\alpha, \beta) = (0.6, 0.9)$ and corresponds to the parameters used in panel (c). In panel (c), point T locates the intersection between (16) and (11), (15), while S_2 is located at $(\sigma_1, \gamma_1) = (0.2, 0.5)$ and corresponds to the parameters used in panel (b). (d and e) The corresponding critical frequencies along the string stability boundaries. The same color coding is used as in Fig. 2. (For interpretation of the references to color in this figure legend, the reader is referred to the web version of this article.)

[s]. Stability charts in the (β,α)-plane are shown in Fig. 4(b) for $\gamma_1 = 0.5, \sigma_1 = 0.2$ [s], $\tau = 0.4$ [s]. The circled line is the plant stability boundary (9), below which the parameters ensure plant stability. The gray string stable region (enveloped by the curves (11, 15, 16 and 17) covers a large portion of realistic driver parameters α and β, showing the robustness of acceleration-based CCC design against variations in driver gains.

Now we investigate the robustness against the increase of the driver reaction time τ. The sections PR, PQ and QR of the string stability boundary in Fig. 4(b) are given by (16), (17), and (11), (15), respectively. The corresponding critical frequencies ω^{cr} are shown in Fig. 4(d). Notice that at the codimension-two points P, Q and R the critical frequency is zero. When τ is increased, the string stable domain decreases, and the points P, Q and R move closer to each other. At the critical reaction time τ_{cr}, they collide at a codimension-three point, and for $\tau > \tau_{cr}$ there exists no combination of gains α and β that can ensure string stability.

Using (11, 15, 16 and 17), we may obtain the location of P, Q, R as

$$\begin{aligned}(\beta_P,\alpha_P) &= ((1-\gamma_1)f^*,0),\\ (\beta_Q,\alpha_Q) &= \left(\frac{\gamma_1^2-1}{2(\gamma_1(\tau-\sigma_1)-\tau)},0\right),\\ (\beta_R,\alpha_R) &= \left(\frac{r_1}{r_3},\frac{r_2}{r_3}\right),\end{aligned} \tag{18}$$

where

$$\begin{aligned}r_1 &= (1-\gamma_1)\left(\gamma_1\left(1-2f^{*2}(\tau-\sigma_1)^2\right)+2f^*\tau(f^*\tau-2)+1\right),\\ r_2 &= (2f^*(\sigma_1-\tau)-1)\gamma_1^2+2f^*(2\tau-\sigma_1)\gamma_1-2f^*\tau+1,\\ r_3 &= \gamma_1(\tau-\sigma_1)(f^*(\tau-\sigma_1)+1)+\tau(1-f^*\tau).\end{aligned} \tag{19}$$

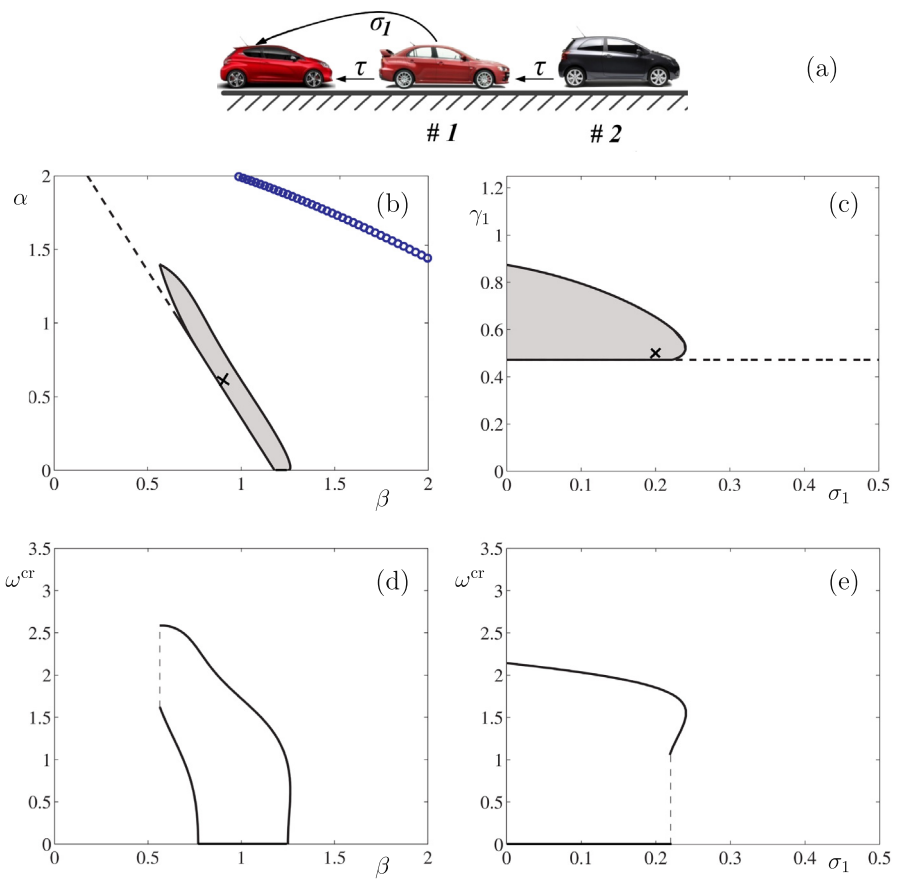

Fig. 5. (a) Connectivity structure with the delays indicated along the links. (b and c) Stability diagrams in the (β,α)-plane and in the (σ_1,γ_1)-plane (the string stable domains are shaded). The cross in panel (b) is located at $(\beta,\alpha) = (0.9, 0.6)$ and corresponds to the parameters chosen in panel (c). Similarly, the cross in panel (c) is located at $(\sigma_1,\gamma_1) = (0.2, 0.5)$ and corresponds to the parameters chosen in panel (b). (d and e) Critical frequencies along the string stability boundaries. For all panels, $\tau = 0.4$ [s] is used. The notation is the same as in Fig. 4, except that the color code is omitted for simplicity. (For interpretation of the references to color in this figure legend, the reader is referred to the web version of this article.)

For $r_2 = 0$, P, Q, and R coincide, which yields the critical driver reaction time

$$\tau_{\rm cr} = \frac{1}{2f^*} + \frac{\gamma_1}{1-\gamma_1}\left(\frac{1}{f^*} - \sigma_1\right) = \frac{t_{\rm h}}{2} + \frac{\gamma_1}{1-\gamma_1}(t_{\rm h} - \sigma_1). \tag{20}$$

Without acceleration feedback ($\gamma_1 = 0$), $\tau_{\rm cr} = \frac{1}{2f^*} = \frac{t_{\rm h}}{2}$, which means that human drivers can only maintain string stability when travelling at a time headway that is at least twice as long as their reaction time. This result also corresponds to the conclusion in Zhang and Orosz (2013); Zhang and Orosz (2014). The second term is positive for the physically realistic parameters $0 < \gamma_1 < 1$ and $\sigma_1 < t_{\rm h}$ and thus the critical delay $\tau_{\rm cr}$ increases with γ_1. In particular, considering $\gamma_1 = 0.5$ without communication delay ($\sigma_1 = 0$ [s]), we have $\tau_{\rm cr} = 3t_{\rm h}/2$, which is a threefold increase. Even if the communication delay is as large as the human reaction time, we have $\tau_{\rm cr} = t_{\rm h}$, which is a twofold increase. This demonstrates the benefits of acceleration-based driver assistance systems.

When $\gamma_1 > 1$, with $\sigma_1 < t_{\rm h}$, we can have $\tau_{\rm cr} < 0$ [s], as in Case G in Fig. 2(e). Finally, when $\gamma_1 \to 1^-$, $\tau_{\rm cr}$ approaches infinity. The cost of such a dramatic increase is the robustness of string stability: α and β both approach zero, resulting in a follower driving with its leader's acceleration (delayed by σ_1). In this case, the headway and velocity feedback terms are missing and thus the vehicle is unable to maintain a velocity-dependent headway.

The available values of the design parameters σ_1 and γ_1 are shown in Fig. 4(c) for human parameters $(\beta, \alpha) = (0.9, 0.6)$ (point S_1 in panel (b)) while the corresponding critical frequencies $\omega^{\rm cr}$ are shown in Fig. 4(e). Since the plant stability is not influenced by acceleration feedback, the choice of human parameters ensures plant stability for all values of σ_1 and γ_1. The string stability boundaries (11, 15 and 16) envelope the gray string stable area, where the point S_2 corresponds to the design parameters used in panel (b). Notice that γ_1 shall be chosen between 0.2 and 0.8 and σ_1 shall be smaller than 0.4 [s] to ensure string stability. According to the coloring, choosing smaller γ_1 leads to string instability at low frequencies, while larger γ_1 or longer σ_1 results in higher-frequency string instabilities.

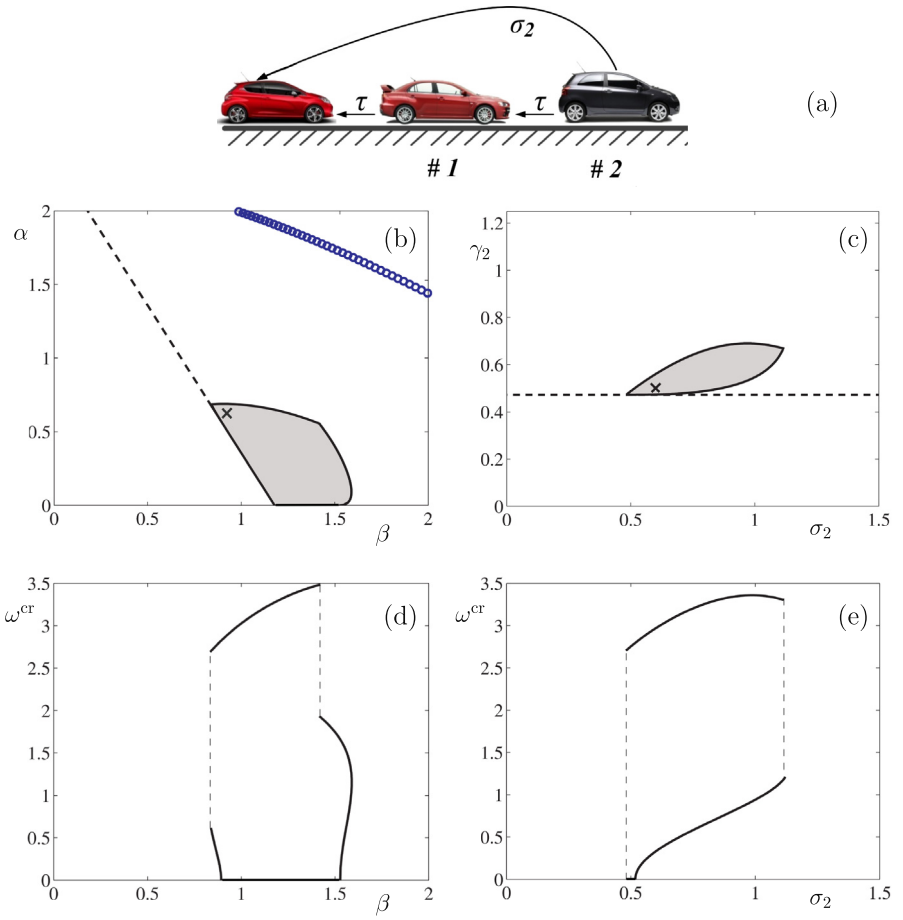

Fig. 6. (a) Connectivity structure with the delays indicated along the links. (b and c) Stability diagram in (β, α)- plane and the (σ_2, γ_2)-plane (the string stable domain is shaded). The cross in panel (b) is located at $(\beta, \alpha) = (0.9, 0.6)$ and corresponds to the parameters chosen in panel (c). Similarly, the cross in panel (c) is located at $(\sigma_2, \gamma_2) = (0.6, 0.5)$ and corresponds to the parameters chosen in panel (b). (d and e) Critical frequencies along the string stability boundaries. For all panels $\tau = 0.4$ [s] is used and the notation is the same as in Fig. 5.

Using $\gamma_1 \approx 0.5$ ensures robustness against the variations of the acceleration delay σ_1. In fact, we will show that $\gamma_1 \approx 0.5$ is a good choice for all other connectivity structures considered in the rest of this paper. Moreover, we will also demonstrate that this holds for all γ_k. While there is no formal proof why this value shall be chosen, this seems to be a compromise between using no acceleration feedback ($\gamma_k = 0$) and using excessive acceleration feedback ($\gamma_k > 1$) which typically leads to high-frequency instabilities.

Note that one may also use a ring configuration to obtain the results shown above, which gives analogous results and also provides an insight into the pattern formation along the road as explained in Appendix A.

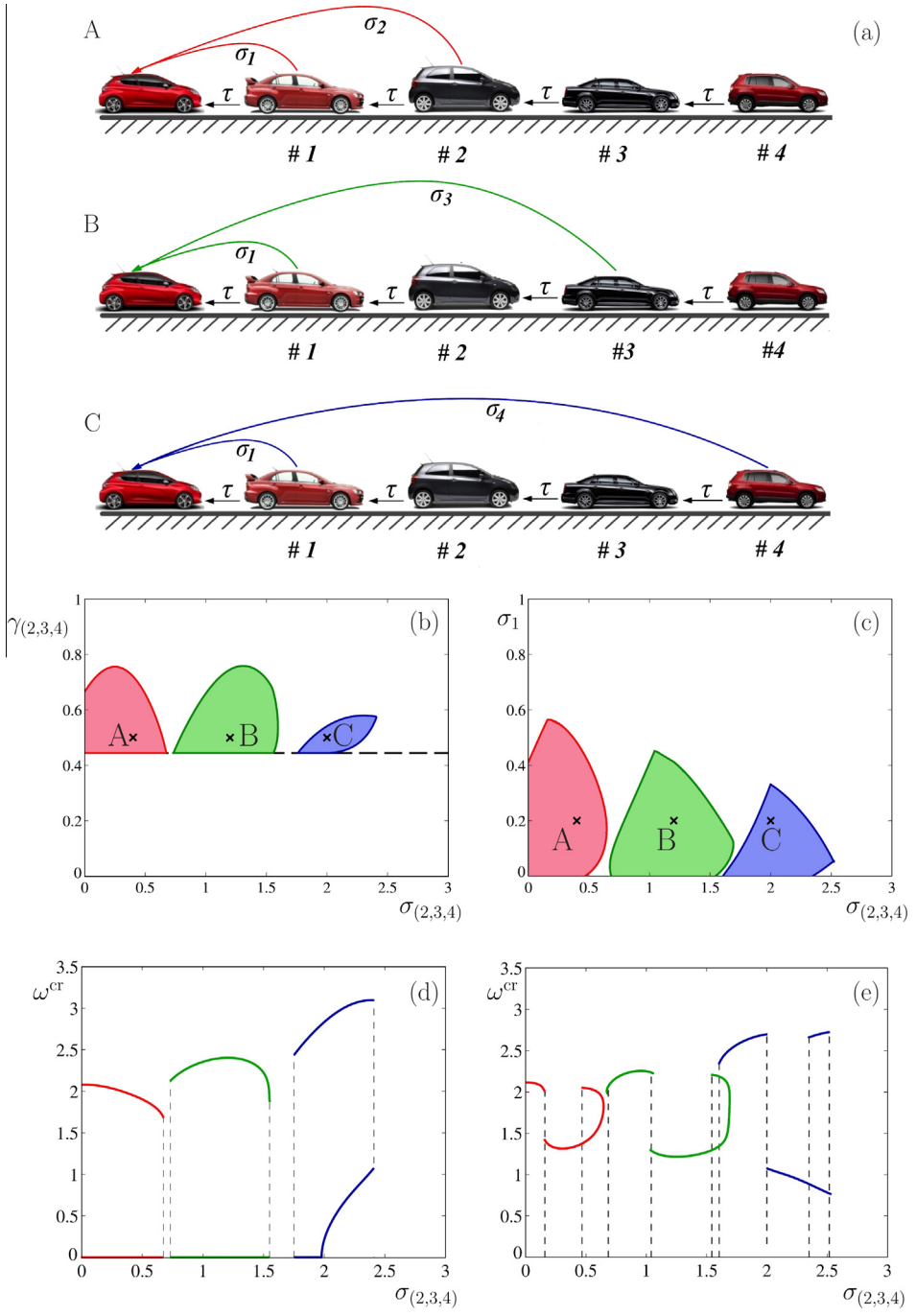

Fig. 7. (a) Three connectivity configurations A, B and C for a five-car platoon with a CCC vehicle at the tail using two acceleration links. The delays are marked along the links. (b and c) String stability diagrams in the (σ_k, γ_k)-plane for $\sigma_1 = 0.2$ [s], $\gamma_1 = 0.5$, and in the (σ_k, σ_1)-plane for $\gamma_1 = \gamma_2 = \gamma_3 = \gamma_4 = 0.5$. The three configurations are indicated by labels and color. (d and e) The critical frequencies along the string stability boundaries. Color code is used to help identify the domains and the frequencies. (For interpretation of the references to color in this figure legend, the reader is referred to the web version of this article.)

3.2. Monitoring two vehicles ahead

Since an advantage of connectivity is providing the host vehicle with non-local information, we consider larger platoons and exploit the use of acceleration feedback from vehicles farther downstream. For simplicity, we start with a platoon where a CCC vehicle follows two other non-CCC vehicles and receives acceleration signals from the vehicle immediately ahead, as shown in Fig. 5(a). Therefore, using $n = 1, m = 1$ in (7) results in the transfer function

$$\Gamma(s) = \left(\frac{F(s)}{G(s)}\right)^2 \left(1 + \frac{F_1(s)}{F(s)}\right). \tag{21}$$

The resulting stability charts are shown in the (β, α)-plane and (σ_1, γ_1)-plane in Fig. 5(b) and (c), respectively. The corresponding critical frequencies are plotted in Fig. 5(d) and (e). The same notation is used as in Fig. 4, but the color code is omitted for simplicity.

When comparing Figs. 4(b) and 5(b), it can be observed that when a CCC vehicle only monitors acceleration information of the vehicle immediately ahead, the longer platoon is more sensitive to uncertainties in the human parameters α and β. Moreover, comparing Figs. 4(c) and 5(c) shows that, while the stable domain is still around $\gamma_1 \approx 0.5$, the domain of feasible control parameters decreases for the larger platoon, including the largest allowable acceleration delay. These results are not surprising: for the larger platoon the CCC vehicle needs to eliminate the perturbations that have been amplified by the human-driven vehicle 1, which is string unstable for $\tau = 0.4$ [s] (for any combination of α and β) since τ is larger than the critical time delay $\tau_{cr} \approx 0.32$ [s], cf. (20) for $\gamma_1 = 0$.

Notice that there are points along the stability boundaries that correspond to multiple critical frequencies. Some of these codimension-two points corresponds to zero frequencies, but there are points where one or both critical frequencies are non-zero. In the latter case, when crossing the string stability boundary at these points (from stable to unstable), stability is lost in two distinct frequency domains and we obtain Bode plots that are qualitatively similar to the one in Fig. 3(f).

If the CCC vehicle receives acceleration feedback from the head vehicle as shown in Fig. 6(a), i.e., $n = 2, m = 0$ in (7), the transfer function becomes

$$\Gamma(s) = \left(\frac{F(s)}{G(s)}\right)^2 \left(1 + \frac{F_2(s)G(s)}{(F(s))^2}\right). \tag{22}$$

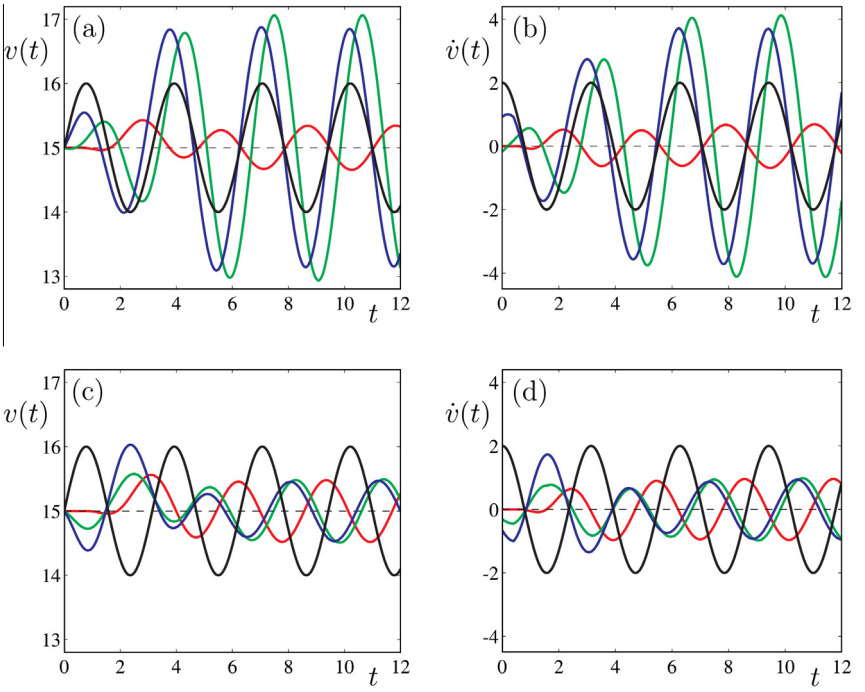

Fig. 8. Velocity and acceleration responses of the CCC vehicle to a sinusoidal velocity perturbation of the head vehicle (black curves) for configurations A (red), B (green), and C (blue) shown in Fig. 7(a). The human parameters α, β, and τ are the same as in Fig. 7 and the acceleration gains are kept $\gamma_k = 0.5$ for all k-s. Panels (a, b) are for acceleration delays $\sigma_k = 0.2$ [s], $k = 1, 2, 3, 4$, while panels (c, d) are for delays $\sigma_1 = 0.2$ [s], $\sigma_2 = 0.4$ [s], $\sigma_3 = 1.2$ [s], $\sigma_4 = 2.0$ [s] (cf. the crosses A, B and C in Fig. 7(b, c)). The initial headways and velocities are set at the equilibrium where $h^* = 20$ [m], $v^* = 15$ [m/s] along the time interval $[-\max\{\sigma_k, \tau\}, 0]$ for all vehicles. (For interpretation of the references to color in this figure legend, the reader is referred to the web version of this article.)

Comparing the string stable areas in Fig. 5(b) and Fig. 6(b), one may observe that using longer acceleration link provides better robustness against uncertainties in the human parameters α and β. The comparison of Fig. 5(b) and Fig. 6(c) reveals that the acceleration feedback gains $\gamma_k, k = 1,\ 2$, shall be kept around 0.5, independent of the source of acceleration signals. Surprisingly, for the longer communication links, the delay in the acceleration feedback loop must be larger than zero. This means that one must artificially increase the delay in order to maintain string stability. Therefore, it is not necessary to use higher communication rate, but instead the received packets shall be stored in buffers, so that they can be used at suitable times. The frequency plots shown in Fig. 6(d, e) are similar to Fig. 5(d, e), but there are multiple codimension-two points with non-zero critical frequencies.

3.3. Using multiple communication links for a CCC vehicle

Because the average broadcast range of DSRC is approximately 300 [m], a CCC vehicle may acquire acceleration information from a car that is approximately four vehicles ahead when driving at highway speed. Thus, here we consider a platoon of five cars, place the CCC vehicle at the tail, and assume that it receives acceleration signals from two other vehicles downstream: the vehicle immediately ahead and another vehicle that is 2, 3, or 4 vehicles ahead; see Fig. 7(a) for the different configurations labelled A, B, and C. Considering these configurations in (7), we obtain the head-to-tail transfer functions

$$\Gamma_{\mathrm{A}}(s) = \left(\frac{F(s)}{G(s)}\right)^4 \left(1 + \frac{F_1(s)}{F(s)} + \frac{F_2(s)G(s)}{(F(s))^2}\right), \tag{23}$$

$$\Gamma_{\mathrm{B}}(s) = \left(\frac{F(s)}{G(s)}\right)^4 \left(1 + \frac{F_1(s)}{F(s)} + \frac{F_3(s)(G(s))^2}{(F(s))^3}\right), \tag{24}$$

$$\Gamma_{\mathrm{C}}(s) = \left(\frac{F(s)}{G(s)}\right)^4 \left(1 + \frac{F_1(s)}{F(s)} + \frac{F_4(s)(G(s))^3}{(F(s))^4}\right). \tag{25}$$

Fig. 7(b,c) show the stability diagrams for $\alpha = 0.6$ [1/s], $\beta = 0.9$ [1/s], $\tau = 0.4$ [s]. Fig. 7(b) depicts the stability charts in the (γ_k, σ_k)-plane for $k = 2, 3, 4$, when $\gamma_1 = 0.5$ and $\sigma_1 = 0.2$ [s]. The different configurations are distinguished by color. Notice again that while γ_k shall be kept around 0.5 for $k = 2, 3, 4$, σ_k shall increase with k to ensure string stability. That is, the controller has to delay acceleration signals coming from distant vehicles, and the longer the link is, the larger delays are needed. Similarly, Fig. 7(c) shows the stability charts in the (σ_k, σ_1)-plane when $\gamma_k = 0.5$ for $k = 1, 2, 3, 4$, using the same labeling and color scheme. While the range of σ_1 is not significantly influenced by the link length, longer links shall have larger delays to

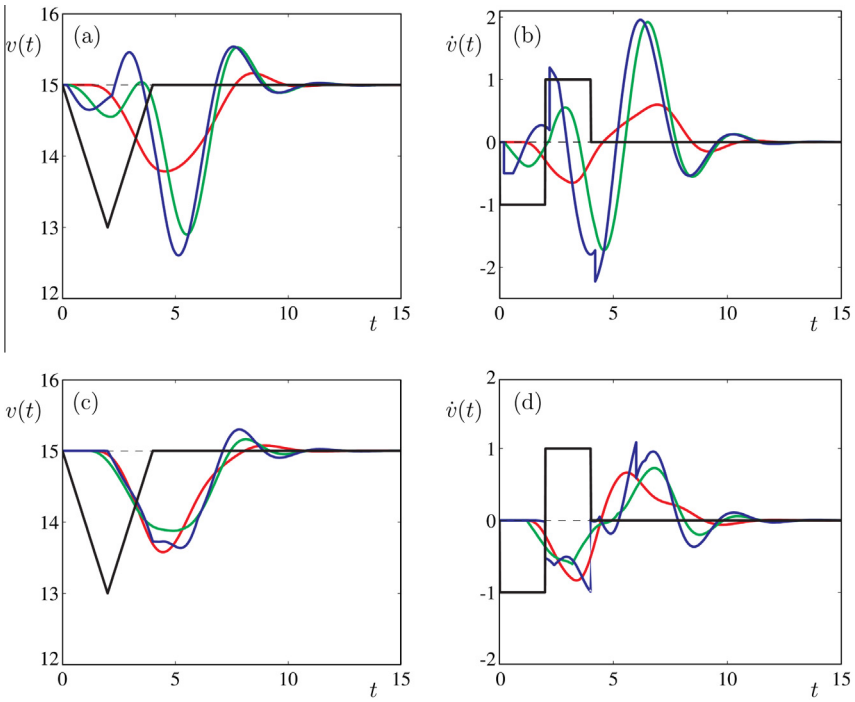

Fig. 9. Velocity and acceleration responses of the CCC vehicle to a triangular velocity perturbation of the head vehicle (black curves) for configurations A (red), B (green), and C (blue) shown in Fig. 7(a). The parameters and initial conditions are the same as in Fig. 8. (For interpretation of the references to color in this figure legend, the reader is referred to the web version of this article.)

maintain string stability. Fig. 7(d,e) give the critical frequencies along the string stability boundaries, showing multiple codimension-two points with two distinct frequencies. Notice that the codimension-two points in Fig. 7(d) have at least one critical frequency at zero, while all codimension-two points in Fig. 7(e) have only non-zero critical frequencies.

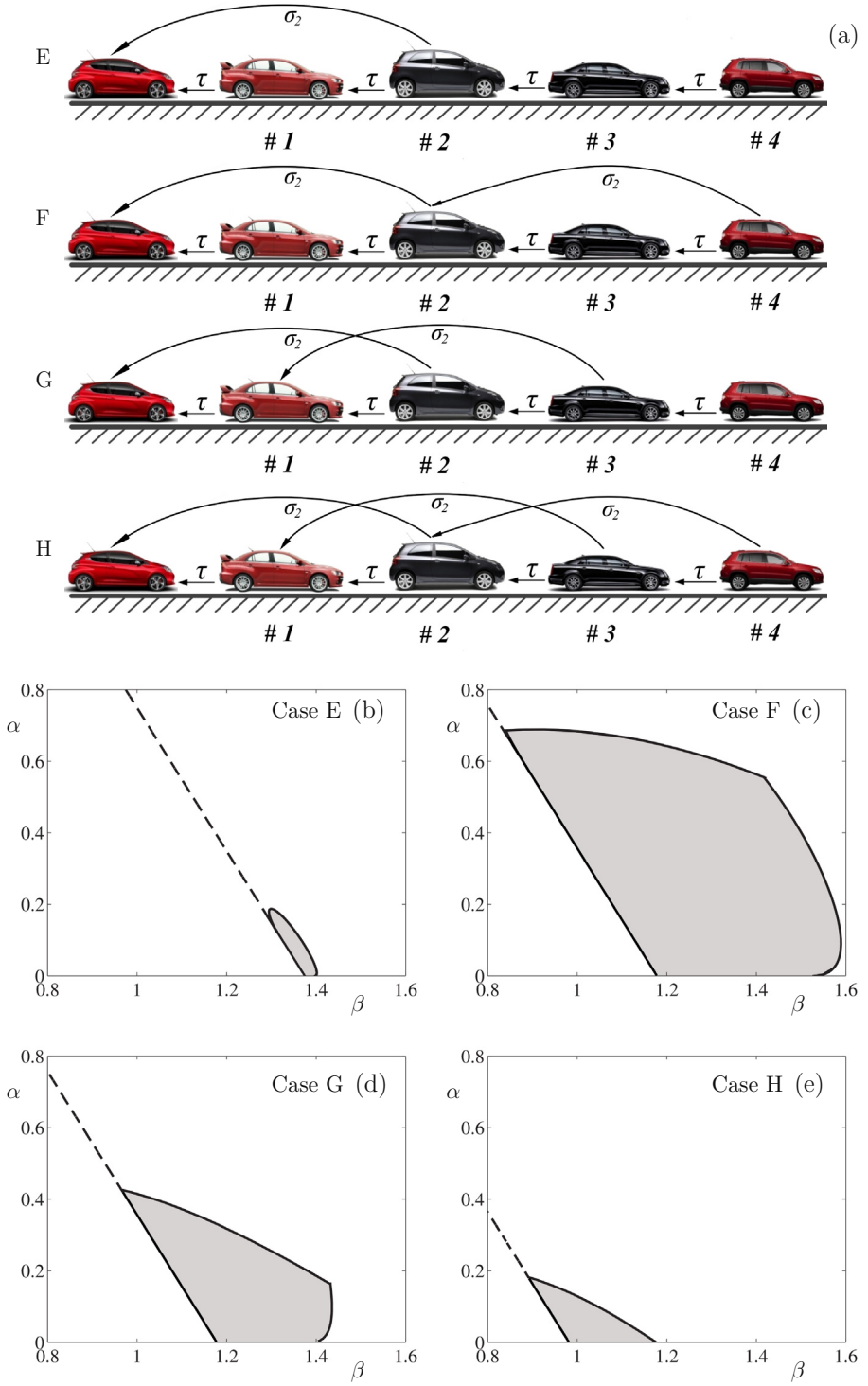

Fig. 10. (a) Four connectivity configurations for a five-car platoon with multiple CCC vehicles and multiple acceleration links. The delays are shown along the links. (b–e) String stability diagrams in the (β, α)-plane for the different configurations while using $\tau = 0.4$ [s], $\gamma_2 = 0.5, \sigma_2 = 0.6$ [s]. The same notation is used as in Fig. 5.

To illustrate the necessity of increasing the delay, we perform simulations for the three configurations A, B and C shown in Fig. 7(a) using the nonlinear model (1, 3). We use the same α, β and τ parameters as in Fig. 7. Fig. 8 depicts the velocity and acceleration responses of the CCC vehicle when all cars in the platoon start with equilibrium headway and velocity along the time interval $[-\max\{\sigma_k, \tau\}, 0]$. The head vehicle applies a periodic perturbation with frequency $\omega = 2$ [rad/s] and amplitude $|\Delta v| = 1$ [m/s] (black curves in Fig. 8). This particular frequency is chosen based on the range of critical frequencies in Fig. 7(d, e). In Fig. 8(a, b), the acceleration delays are kept the same for all links, that is, $\sigma_k = 0.2$ [s], $\gamma_k = 0.5, k = 1, 2, 3, 4$. Case A (red curve) is string stable, i.e., the amplitude of the steady-state velocity response is smaller than the amplitude of the disturbance (black curve). However, cases B (green curve) and C (blue curve) are not string stable as the velocity disturbance is amplified. Fig. 8(c, d) show the velocity and acceleration responses when the acceleration delays are increased with link length. In particular, we choose $\sigma_1 = 0.2$ [s], $\sigma_2 = 0.4$ [s], $\sigma_3 = 1.2$ [s], $\sigma_4 = 2.0$ [s] and $\gamma_k = 0.5, k = 1, 2, 3, 4$, corresponding to the crosses in Fig. 7(b, c). In this setting, all three configurations are string stable, i.e., the velocity perturbations for the red, green and blue curves are all smaller compared to the black curve. This is consistent with results of the linear analysis presented above.

To further emphasize this principle, Fig. 9 shows the velocity and acceleration responses when the head vehicle has a triangular velocity perturbation between $t \in [0, 4]$ [s] with perturbation size $|\Delta v| = 2$ [m/s] (black curves in Fig. 9). Since the triangular signal can be written as a sum of Fourier components, and is more common in real traffic than pure sinusoidal signals, the attenuation of triangular perturbation may be considered as an indication of string stability. In Fig. 9(a, b), we have $\sigma_k = 0.2$ [s], for $k = 1, 2, 3, 4$, and the perturbation is only attenuated in case A but amplified in cases B and C. On the other hand, panels (c, d) are for $\sigma_1 = 0.2$ [s], $\sigma_2 = 0.4$ [s], $\sigma_3 = 1.2$ [s], $\sigma_4 = 2.0$ [s], and the perturbation is attenuated in all cases. These simulation results demonstrate that near the equilibrium, the nonlinear model reproduces the predictions of the linear analysis.

3.4. Multiple CCC vehicles: effects of link intersections

As seen in the last section, multiple links may be used to improve string stability when there is a CCC vehicle in the platoon. However, when more than one CCC vehicles appear, complicated connectivity structures may arise. In this section, we demonstrate that increasing the number of links may not always provide larger string stability domains.

Here we consider a five-car platoon and compare the head-to-tail string stability in configurations E–H depicted in Fig. 10(a). In each case, we use links that allow CCC vehicles to obtain acceleration information from a vehicle that is two vehicles ahead and choose the parameters for this acceleration link to be $\gamma_2 = 0.5, \sigma_2 = 0.6$ [s], cf. the cross in Fig. 6(c). Notice that the number of links increases when going from E to H. The corresponding (β, α) stability charts are shown in Fig. 10(b-e). Since we still consider $\tau = 0.4$ [s] as in Fig. 7, without acceleration feedback the platoon is string unstable. In case E, the CCC vehicle at the tail can make the platoon head-to-tail string stable, though the stable domain is fairly small as shown in Fig. 10(a). Case F is a cascade configuration with two CCC vehicles involved and the corresponding string stable domain is identical to the one in Fig. 6 (a). In case G, there are two CCC vehicles, but the two links intersect each other and the stability region shrinks significantly as shown in Fig. 10(d). This result indicates that intersection of acceleration links may deteriorate string stability. Finally, to investigate whether the stabilizing effect of acceleration links outweighs the destabilizing effect of link intersections, we consider three CCC vehicles with three acceleration links in case H. The corresponding stability plot in Fig. 10(e) shows that, surprisingly, the stable domain becomes much smaller. These results suggest that CCC vehicles shall use the available acceleration signals in a selective manner, to avoid link intersections which deteriorate string stability.

4. Conclusion

In this paper, we found that connected cruise control (CCC) that is based on acceleration signals can improve the string stability of vehicle platoons and that CCC can be used in human-driven vehicles without instrumenting them with expensive sensors. Such improvements are robust against driver reaction time and communication delay. We observed that the critical driver reaction time increases significantly when using appropriately designed acceleration feedback. We also demonstrated that the gain of the acceleration feedback shall be kept around 0.5 at all circumstances. Having too low acceleration gains would lead to low frequency oscillations (that are typical for human driven platoons), while too high acceleration gains lead to high frequency string instabilities. As the length of acceleration feedback link increases, the corresponding delay time shall also be increased, in order to maintain string stability. This indicates a necessity of designing the delay times when using acceleration feedback, instead of treating the delays as system limitations. Furthermore, we showed that string stability can be preserved when building larger connected vehicle systems, under the condition that link intersections are avoided. In the future, optimization of acceleration gains for different link lengths and heterogeneity arising from non-identical human reaction times shall be considered.

Appendix A

Here we show that the necessary and sufficient conditions of string stability for a platoon are equivalent to the stability conditions of the system constructed by placing N vehicles on a ring and considering $N \to \infty$. That is, the string stability of a

platoon of CCC and non-CCC vehicles (cf. Fig. 1(a)) can be analyzed by repeating the configuration along a circular track. This setting introduces periodic boundary conditions and results in an autonomous system. Previous research has shown the equivalence of the ring and platoon configurations for predecessor-follower models based on headway and velocity feedback (Orosz et al., 2011). Here we give a brief demonstration of their equivalency for connected vehicle systems with delayed acceleration feedback. First, we analyze the simple scenario discussed in Section 3.1 where only the acceleration of the vehicle immediately ahead is used and then extend this analysis to the platoons discussed in Sections 3.2 and 3.4.

Let us define

$$x = \begin{bmatrix} \tilde{v} \\ \tilde{h} \end{bmatrix}, \quad x_1 = \begin{bmatrix} \tilde{v}_1 \\ \tilde{h}_1 \end{bmatrix}, \tag{26}$$

consider $n = 1$ and write the linear model (5) into the form

$$\dot{x}(t) = \mathbf{A}\, x_1(t) + \mathbf{B}\, x(t) + \mathbf{C}\, x_1(t-\tau) + \mathbf{D}\, x(t-\tau) + \mathbf{E}\, \dot{x}_1(t-\sigma_1), \tag{27}$$

where the coefficient matrices are

$$\mathbf{A} = \begin{bmatrix} 0 & 0 \\ 1 & 0 \end{bmatrix}, \quad \mathbf{B} = \begin{bmatrix} 0 & 0 \\ -1 & 0 \end{bmatrix}, \quad \mathbf{C} = \begin{bmatrix} \beta & 0 \\ 0 & 0 \end{bmatrix}, \quad \mathbf{D} = \begin{bmatrix} -\alpha-\beta & \alpha f^* \\ 0 & 0 \end{bmatrix}, \quad \mathbf{E} = \begin{bmatrix} \gamma_1 & 0 \\ 0 & 0 \end{bmatrix}. \tag{28}$$

Placing N vehicles on a ring and defining the state $X = \mathrm{col}[x_1 \ \cdots \ x_N]$ result in the neutral delay differential equation (NDDE)

$$\dot{X}(t) = \begin{bmatrix} \mathbf{B} & \mathbf{A} & & \\ & \ddots & \ddots & \\ & & \mathbf{B} & \mathbf{A} \\ \mathbf{A} & & & \mathbf{B} \end{bmatrix} X(t) + \begin{bmatrix} \mathbf{D} & \mathbf{C} & & \\ & \ddots & \ddots & \\ & & \mathbf{D} & \mathbf{C} \\ \mathbf{C} & & & \mathbf{D} \end{bmatrix} X(t-\tau) + \begin{bmatrix} \mathbf{0} & \mathbf{E} & & \\ & \ddots & \ddots & \\ & & \mathbf{0} & \mathbf{E} \\ \mathbf{E} & & & \mathbf{0} \end{bmatrix} \dot{X}(t-\sigma_1). \tag{29}$$

Block-diagonalizing (29), we can decompose it into N modal equations, which can be analyzed separately (Ge et al., 2013; Avedisov and Orosz, 2014). The dynamics of the k^{th} mode is given by

$$\dot{z}_k(t) = (\mathbf{B} + \Lambda_k\, \mathbf{A})\, z_k(t) + (\mathbf{D} + \Lambda_k\, \mathbf{C})\, z_k(t-\tau) + \Lambda_k\, \mathbf{E}\, \dot{z}_k(t-\sigma_1), \tag{30}$$

where $z_k \in \mathbb{R}^2$ is the modal coordinate for the k^{th} mode representing the amplitude of the corresponding traveling wave (Orosz et al., 2010), while

$$\Lambda_k = \mathrm{e}^{2\mathrm{i}\theta_k}, \quad \theta_k = \frac{k\pi}{N}, \tag{31}$$

$k = 0, \ldots, N-1$ are the corresponding modal eigenvalues.

Using the trial solution $z_k = Z_k\, \mathrm{e}^{st}$, $Z_k \in \mathbb{C}^2$, $s \in \mathbb{C}$, we obtain the characteristic equation for the k^{th} mode as

$$s^2\left(1 - \gamma_1\, \mathrm{e}^{2\mathrm{i}\theta_k - s\sigma_1}\right) + s\left(\alpha + \beta\left(1 - \mathrm{e}^{2\mathrm{i}\theta_k}\right)\right) \mathrm{e}^{-s\tau} + \alpha f^*\left(1 - \mathrm{e}^{2\mathrm{i}\theta_k}\right) \mathrm{e}^{-s\tau} = 0. \tag{32}$$

The necessary and sufficient condition of stability is that all modes are stable, that is, all eigenvalues s are in the left-half complex plane for all k (Insperger and Stépán, 2011). The stability boundaries are located at the parameter values where eigenvalues cross the imaginary axis, i.e., $s = \mathrm{i}\omega, \omega \geqslant 0$. Substituting this into (32) and separating the real and imaginary parts, we obtain

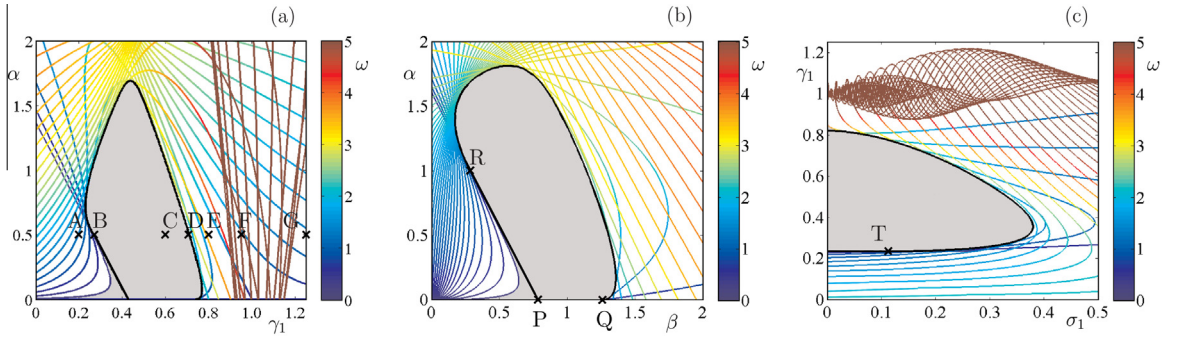

Fig. 11. (a) Stability chart in the (γ_1, α)-plane for the ring configuration using $N = 33$ vehicles and the same parameters as in Fig. 2(e). (b and c) Stability charts in the (β, α) and (σ_1, γ_1) planes for the ring configuration using $N = 33$ vehicles and the same parameters as in Fig. 4(a, b). Each colored curve represents a stability boundary for a mode (a traveling wave along the ring) and the color describes the frequency of arising oscillations at the boundaries. The black lines are the string stability boundaries obtained when analyzing platoon configuration. (For interpretation of the references to color in this figure legend, the reader is referred to the web version of this article.)

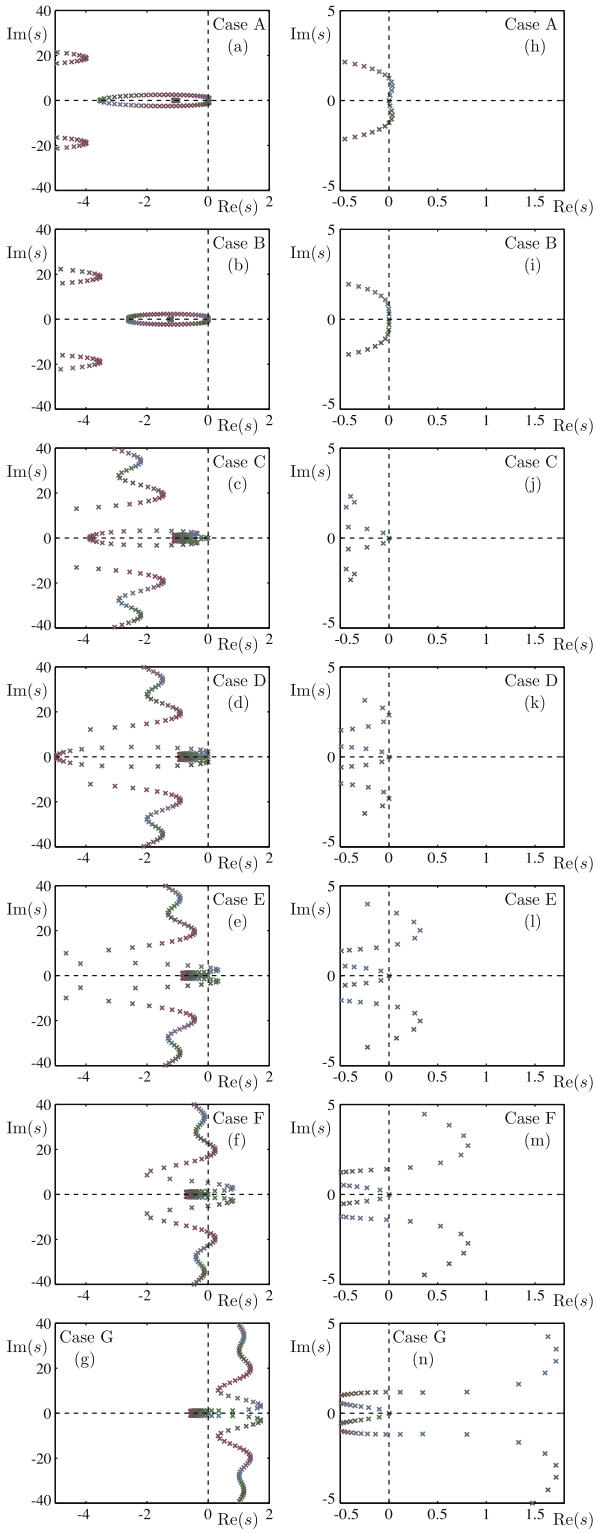

Fig. 12. (a–g) Eigenvalue distributions for the ring configuration for the points A–G in Fig. 11(c). (h–n) The zoom-ins for panels (a–g). The color of eigenvalues changes from blue through purple to green as the mode number $k = 0, \ldots, 32$ increases. (For interpretation of the references to color in this figure legend, the reader is referred to the web version of this article.)

$$R(\omega) - \gamma_1 \omega^2 \cos(2\theta_k - \sigma_1 \omega) = 0,$$
$$T(\omega) - \gamma_1 \omega^2 \sin(2\theta_k - \sigma_1 \omega) = 0, \tag{33}$$

where

$$R(\omega) = \omega^2 - \alpha\omega \sin(\tau\omega) - 2\sin(\theta_k)(\beta\omega \cos(\theta_k - \tau\omega) + \alpha f^* \sin(\theta_k - \tau\omega)),$$
$$T(\omega) = -\alpha\omega \cos(\tau\omega) - 2\sin(\theta_k)(\beta\omega \sin(\theta_k - \tau\omega) + \alpha f^* \cos(\theta_k - \tau\omega)). \tag{34}$$

Solving (33,34) for α and γ_1, we obtain the stability boundaries in the parametric form

$$\alpha = \frac{\omega^2 \sin(2\theta_k - \sigma_1\omega) - 2\beta\omega \sin(\theta_k)\sin(\theta_k + (\tau - \sigma_1)\omega)}{2f^* \sin(\theta_k)\cos(\theta_k + (\tau - \sigma_1)\omega) - \omega\cos(2\theta_k + (\tau - \sigma_1)\omega)},$$
$$\gamma_1 = \frac{R(\omega)}{\omega^2 \cos(2\theta_k - \sigma_1\omega)}, \tag{35}$$

for $k = 0, \ldots, N-1$. Similarly one may solve (33,34) for α and β and obtain

$$\alpha = \frac{\omega^2 \sin(2\theta_k - \sigma_1\omega) - 2\beta\omega \sin(\theta_k)\sin(\theta_k + (\tau - \sigma_1)\omega)}{2f^* \sin(\theta_k)\cos(\theta_k + (\tau - \sigma_1)\omega) - \omega\cos(2\theta_k + (\tau - \sigma_1)\omega)},$$
$$\beta = \frac{\omega\cos(2\theta_k + (\tau - \sigma_1)\omega) - 2f^* \sin(\theta_k)\cos(\theta_k + (\tau - \sigma_1)\omega) + (2f^* \sin(\theta_k)\cos(\theta_k - \tau\omega) - \omega\cos(\tau\omega))/\gamma_1}{2\sin(\theta_k)(2f^* \sin(\theta_k) - \omega\cos(\theta_k))/(\gamma_1\omega)}, \tag{36}$$

for $k = 0, \ldots, N-1$. Finally, solving (33,34) for σ_1 and γ_1, we obtain

$$\sigma_1 = \frac{1}{\omega}\left(2\theta_k - \arctan\left(\frac{T(\omega)}{R(\omega)}\right)\right),$$
$$\gamma_1 = \frac{R(\omega)}{\omega^2 \cos(2\theta_k - \sigma_1\omega)}, \tag{37}$$

for $k = 0, \ldots, N-1$. The corresponding stability diagrams are shown in the $(\gamma_1, \alpha), (\beta, \alpha), (\sigma_1, \gamma_1)$ planes in Fig. 11(a, b, c), respectively. In all three panels, the gray areas are stable and each colored curve is a stability boundary for a mode number k. Black curves indicate the string stability boundaries obtained for the platoon configuration (cf. Figs. 2(e) and 4(b, c)). Clearly, the stability areas for the ring configuration match with those for the platoon configuration, except for a small corner in the low frequency part. Because there are only a finite number of vehicles on the ring ($N = 33$ is used here), the continuum of frequencies in the string unstable domain are "sampled" by a finite number of modes. This is demonstrated using similar coloring in Fig. 11 as in Figs. 2(e) and 4(b,c). When the number of vehicles in the ring is increased, the discrepancy between platoon and the ring diminishes.

Fig. 12 shows the eigenvalue distribution for the points marked A–G in Fig. 11(a) using the semi-discretization method (Insperger and Stépán, 2011). They correspond to the Bode plots in Fig. 3. Since (29) is a neutral delayed differential equation (NDDE), there are infinitely many eigenvalues. We only plot the eigenvalues close to the imaginary axis, which dominate the dynamics. Case C is asymptotically stable, because all the eigenvalues are on the left-half complex plane. Cases B and D are marginally stable, with a pair of eigenvalues crossing the imaginary axis. The crossing frequencies are very close to the critical frequencies ω^{cr} in Fig. 3(b) and (d). In case A, eigenvalues with small imaginary values are on the right-half complex plane, indicating instabilities for low frequencies, while in case E, eigenvalues with larger imaginary parts crossed the

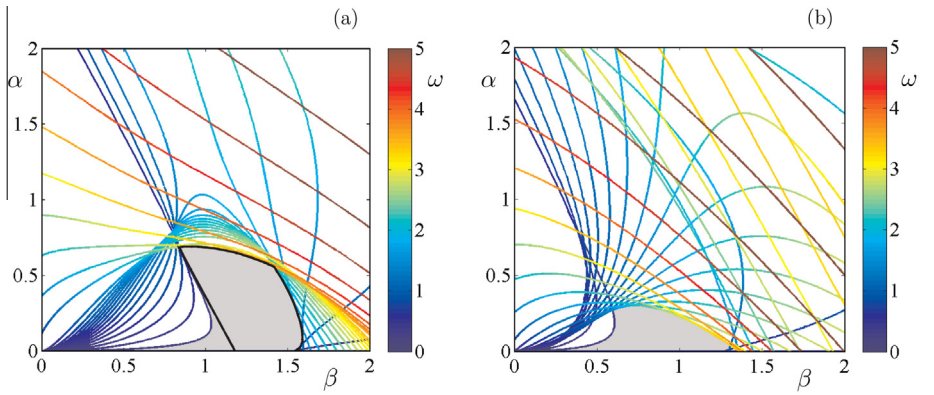

Fig. 13. Stability diagrams in the (β, α)-plane for the ring configuration using $N = 32$ vehicles. (a) Every second vehicle is equipped with acceleration-based CCC, cf. Fig. 6(a) and configuration F in Fig. 10(a). The black lines are the string stability boundaries obtained when analyzing the platoon configuration. (b) Every vehicle is CCC and all acceleration links intersect, cf. Fig. 6(a) and configuration H in Fig. 10(a).

imaginary axis, resulting in instabilities with higher frequencies. In case F, both low frequency and high frequency instabilities occur and in case G, there are infinitely many eigenvalues on the right-half complex plane. We remark that the appearance of such 'hyperbolic-like' spectrum in a dissipative system may reconcile the conflict that arose for the continuum traffic models, regarding whether the model should be fundamentally hyperbolic (Aw and Rascle, 1999) or parabolic (Daganzo, 1995).

Stability analysis for more general connectivity structures can be done by placing the platoons on a ring repetitively. Here we show that the intersection of acceleration links for the ring configuration generates similar results as for the platoon configuration. Fig. 13 compares the stability in the (β, α)-plane between two 32-vehicle rings. Panel (a) depicts the stability chart when 16 CCC vehicles are evenly distributed in the ring of 32 vehicles and acceleration links do not intersect, see configuration F in Fig. 10(a). Panel (b) shows the stability chart when 32 vehicles are all equipped with CCC, and the connectivity is similar to configuration H in Fig. 10(a). Even though the number of acceleration links in panel (a) is half the number in panel (b), the stable area is significantly larger. The stable domain in Fig. 13(a) matches the string stability boundary obtained for the platoon configuration in Fig. 6(c), except a corner in the low-frequency area; see black curves for comparison. Such difference diminishes when increasing the number of vehicles on the ring. Also, the stability chart in Fig. 13(b) resembles the chart in Fig. 10(e). Again, by increasing the number of vehicles in the platoon as well as on the ring, better match can be obtained.

References

Avedisov, S.S., Orosz, G., 2014. Nonlinear network modes of circulant systems with applications to connected vehicles. J. Nonlinear Sci., submitted.

Aw, A., Rascle, M., 1999. Resurrection of second order models of traffic flow? SIAM J. Appl. Math. 60 (3), 916–938.

Bai, F., Krishnan, H., 2006. Reliability analysis of DSRC wireless communication for vehicle safety applications. In: IEEE Intelligent Transportation Systems Conference, pp. 355–362.

Chan, E., Gilhead, P., Jelinek, P., Krejci, P., Robinson, T., 2012. Cooperative control of SARTRE automated platoon vehicles. In: Proceedings of the 19th ITS World Congress.

Daganzo, C.F., 1995. Requiem for second-order fluid approximations of traffic flow. Trans. Res. Part B: Methodol. 29 (4), 277–286.

Davis, L.C., 2004. Effect of adaptive cruise control systems on traffic flow. Phys. Rev. E 69 (6), 066110.

Engelborghs, T.K., Samaey, G., 2001. DDE-BIFTOOL v. 2.00: a Matlab package for bifurcation analysis of delay differential equations, Technical Report TW-330, Department of Computer Science, K.U.Leuven, Leuven, Belgium.

Ge, J.I., Avedisov, S.S., Orosz, G., 2013. Stability of connected vehicle platoons with delayed acceleration feedback. In: Proceedings of the ASME Dynamical Systems and Control Conference, ASME, p. V003T30A006 (paper no. DSCC2013-4040).

Geiger, A., Lauer, M., Moosmann, F., Ranft, B., Rapp, H., Stiller, C., Ziegler, J., 2012. Team AnnieWAY's entry to the 2011 grand cooperative driving challenge. IEEE Trans. Intell. Transp. Syst. 13 (3), 1008–1017.

Insperger, T., Stépán, G., 2011. Semi-Discretization for Time Delay Systems. Springer.

Insperger, T., Milton, J., Stépán, G., 2013. Acceleration feedback improves balancing against reflex delay. J. R. Soc. Interface 10 (79), 20120763.

Lidström, K., Sjöberg, K., Holmberg, U., Andersson, J., Bergh, F., Bjäde, M., Mak, S., 2012. A modular CACC system integration and design. IEEE Trans. Intell. Transp. Syst. 13 (3), 1050–1061.

Orosz, G., 2014. Connected cruise control: modeling, delay effects, and nonlinear behavior. Vehicle Syst. Dyn., submitted.

Orosz, G., Shah, S.P., 2012. A nonlinear modeling framework for autonomous cruise control. In: Proceedings of the ASME Dynamic Systems and Control Conference, 2012. DSCC2012. ASME, pp. 467–471.

Orosz, G., Wilson, R.E., Stépán, G., 2010. Traffic jams: dynamics and control. Philos. Trans. R. Soc. A 368 (1928), 4455–4479.

Orosz, G., Moehlis, J., Bullo, F., 2011. Delayed car-following dynamics for human and robotic drivers. In: Proceedings of the ASME IDETC/CIE Conference, ASME, pp. 529–538 (paper no. DETC2011-48829).

Qin, W.B., Orosz, G., 2013. Digital effects and delays in connected vehicles: linear stability and simulations. In: Proceedings of the ASME Dynamical Systems and Control Conference, ASME, p. V003T30A001 (paper no. DSCC2013-3830).

Qin, W.B. Gomez, M.M., Orosz, G., 2014. Stability analysis of connected cruise control with stochastic delay. In: Proceedings of American Control Conference.

Rajamani, R., Shladover, S., 2001. An experimental comparative study of autonomous and co-operative vehicle-follower control systems. Trans. Res. Part C: Emerging Technol. 9 (1), 15–31.

Schrank, D., Eisele, B., Lomax, T., 2012. Annual Urban Mobility Report, Progressreport 70, Texas Transportation Institute, College Station, TX.

Seiler, P., Pant, A., Hedrick, K., 2004. Disturbance propagation in vehicle strings. IEEE Trans. Auto. Control 49 (10), 1835–1842.

van Arem, B., van Driel, C., Visser, R., 2006. The impact of cooperative adaptive cruise control on traffic-flow characteristics. IEEE Trans. Intell. Trans. Syst. 7 (4), 429–436.

van Nunen, E., Kwakkernaat, R., Ploeg, J., Netten, B., 2012. Cooperative competition for future mobility. IEEE Trans. Intell. Trans. Syst. 13 (3), 1018–1025.

Wang, M., Daamen, W., Hoogendoorn, S.P., van Arem, B., 2014a. Rolling horizon control framework for driver assistance systems. part I: mathematical formulation and non-cooperative systems. Trans. Res. Part C: Emerging Technol. 40, 271–289.

Wang, M., Daamen, W., Hoogendoorn, S.P., van Arem, B., 2014b. Rolling horizon control framework for driver assistance systems. part II: cooperative sensing and cooperative control. Trans. Res. Part C: Emerging Technol. 40, 290–311.

Zhang, L., Orosz, G., 2014. Motif-based analysis of connected vehicle systems: delay effects and stability. Automatica, submitted..

Zhang, L., Orosz, G., 2013. Designing network motifs in connected vehicle systems: delay effects and stability. In: Proceedings of the ASME Dynamical Systems and Control Conference, ASME, p. V003T42A006 (paper no. DSCC2013-4081).